Seventh International Conference on Computational Fluid Dynamics (ICCFD7), Big Island, Hawaii, July 9-13, 2012

ICCFD7-3801

Simulations of Compressible Rayleigh-Taylor Instability Using the Adaptive Wavelet Collocation Method

S.J. Reckinger*, D. Livescu**, and O.V. Vasilyev*
Corresponding author: scott.reckinger@colorado.edu

* University of Colorado Boulder, USA.
** Los Alamos National Laboratory, USA.

Abstract: Numerical simulations of the compressible Rayleigh-Taylor instability are performed on an adaptive mesh using the Adaptive Wavelet Collocation Method (AWCM). Due to the physics-based adaptivity and direct error control of the method, AWCM is ideal for resolving the wide range of scales present in the development of the instability. The problem is initialized consistent with the solutions from linear stability theory, with a background state of two diffusively mixed, stratified fluids of differing molar masses. Of interest are the compressibility effects on the departure time from the linear growth, the onset of strong non-linear interactions, and the late-time behavior of the fluid structures. The late time bubble and spike velocities are computed and compared to those obtained in the incompressible case.

Keywords: Rayleigh-Taylor Instability, Adaptive Wavelet Collocation Method, Compressibility, Stratification

1 Introduction

The Rayleigh-Taylor instability (RTI) occurs whenever a low density fluid accelerates into a higher density fluid. A commonly studied RTI system involves a light fluid lying underneath, and thus supporting, a heavier fluid in the presence of gravity [1, 2, 3]. The lighter fluid rises into the heavier fluid in the form of bubbles, while a spike of heavier fluid falls into the lighter fluid as the system seeks to reduce the combined potential energy of the two fluids. Small perturbations at the interface between the high density and low density fluids evolve from early-time linear growth, to late-time non-linear growth of the bubble and spike structures, and eventually a turbulent mixing layer develops [4].

RTI can be observed in a wide range of astrophysical and atmospheric flows [5, 6] and has drastic effects on many engineering systems of interest, such as inertial confinement fusion [7, 8]. The majority of the systems where RTI naturally occurs involve highly compressible fluids. Of particular interest is the crucial role Rayleigh-Taylor mixing plays during the thermonuclear flame front acceleration in type Ia supernovae [9]. Whereas most previous investigations of RTI have focused on the incompressible case, the compressibility effects during this violent expansion are potentially drastic. Thus, a detailed understanding of the compressibility effects on the growth of RTI is necessary. Linear stability theory has shown that there is no unique parameter characterizing compressibility [10]. Acoustic effects, material properties, and background stratification can all affect the instability growth, often in opposed ways. At late times, as the nonlinear effects become important, the number of these parameters is only expected to increase and their interactions to become even more complicated.

An investigation of compressible RTI requires the use of efficient numerical methods, advanced boundary conditions, and a consistent initialization in order to capture the wide range of scales present in the system while reducing the computational impact associated with acoustic wave generation and the subsequent interaction with the flow. Numerical simulations are performed on an adaptive mesh using the Adaptive Wavelet Collocation Method (AWCM). The combined effects of compressibility and large density variations on the late-time behavior of RTI is not currently fully understood [11, 12]. For thermal equilibrium, acoustic and stratification properties of the background flow are interrelated, with stratification itself playing an important role. In order to capture the late time behavior, simulations need to be performed in long vertical domains, with density ranges spanning many orders of magnitude. The utilization of AWCM for simulations on such domains minimizes the computational effort, since Rayleigh-Taylor instability remains a spatially localized phenomenon near the interface well into the turbulent stage. In addition, non-reflecting characteristics-based boundary conditions for a highly stratified hydrostatic background state have been developed to isolate the instability growth from acoustic waves generated at the interface during the growth of compressible RTI.

2 Problem Statement

The compressibility effects at various interfacial density differences are investigated using a two-dimensional, single-mode RTI system. The problem is initialized consistent with the solutions from linear stability theory, with two diffusively mixed, stratified fluids of differing molar masses as the background state. The background stratification depends on both the compressibility of each fluid and the density difference at the interface.

2.1 Governing Equations

Simulations of two-dimensional, single-mode, miscible Rayleigh-Taylor instability are performed by solving the compressible Navier-Stokes, energy, and species mass fraction, Y_l, with $l = \overline{1,2}$, transport equations. Along with the ideal gas equation of state, $P = \rho RT$, the governing equations are as follows [13]:

$$\frac{\partial \rho}{\partial t} + \frac{\partial \rho u_j}{\partial x_j} = 0, \tag{1}$$

$$\frac{\partial \rho u_i}{\partial t} + \frac{\partial \rho u_i u_j}{\partial x_j} = -\frac{\partial p}{\partial x_i} - \rho g_i + \frac{\partial \tau_{ij}}{\partial x_j}, \tag{2}$$

$$\frac{\partial \rho e}{\partial t} + \frac{\partial \rho e u_j}{\partial x_j} = -\frac{\partial p u_i}{\partial x_i} - \rho u_i g_i + \frac{\partial \tau_{ij} u_i}{\partial x_j} + \frac{\partial}{\partial x_j}\left(k \frac{\partial T}{\partial x_j}\right) + \frac{\partial}{\partial x_j}\left(D \rho c_{p_l} T \frac{\partial Y_l}{\partial x_j}\right), \tag{3}$$

$$\frac{\partial \rho Y_l}{\partial t} + \frac{\partial \rho Y_l u_j}{\partial x_j} = \frac{\partial}{\partial x_j}\left(D \rho \frac{\partial Y_l}{\partial x_j}\right), \tag{4}$$

where ρ is the density, P is the pressure, T is the temperature, R is the gas constant, u_i is the velocity in the x_i direction, the specific total energy is defined as $e = u_i u_i/2 + c_p T - P/\rho$, and repeated indices assume summation. The shear stress tensor, assuming Newtonian fluids, is defined as $\tau_{ij} = \mu\left[\partial u_i/\partial x_j + \partial u_j/\partial x_i - (2/3)(\partial u_k/\partial x_k)\delta_{ij}\right]$. Fluid properties, such as the dynamic viscosity, μ, heat conduction coefficient, k, specific heats at constant pressure and volume, c_p and c_v, and mass diffusion coefficient, D, are defined as linear combinations of the individual species' properties using the mass fractions. For example, the specific heat at constant pressure is defined as $c_p = c_{p_l} Y_l$, where summation over repeated indices is used. The system is composed of a heavy fluid lying on top of a lighter fluid in the vertical (x_1) direction. The top fluid molar mass is greater than that for the lower fluid, that is $W_1 > W_2$. Initially, the pressure and the temperature at the interface are P_I and T_I. The length scale used to nondimensionalize the equations is the perturbation wavelength, λ, for the initial interface. The Atwood number, which is a measure of the difference in the densities of the two fluids at the interface, is defined as:

$$A = \frac{W_1 - W_2}{W_1 + W_2}. \tag{5}$$

In order to investigate compressibility effects, a distinction is made between fluid compressibility characterized by the values of the ratios of the specific heats, γ_1 and γ_2, and compressibility effects in response to the thermodynamic state of the system, characterized by a Mach number defining the size of a characteristic velocity relative to the speed of sound [10]. Since the flow starts with zero velocity, the Mach number is defined based on the gravity wave speed, which characterizes the instability driving force, and the isothermal speed of sound, which removes the effects of the specific heats from the definition [10, 14]. The definition is:

$$M = \sqrt{\frac{\rho_I g \lambda}{P_I}}, \tag{6}$$

where $\rho_I = (W_1 + W_2)P_I/(2\mathcal{R}T_I)$, with $\mathcal{R}$ being the universal constant, is the fluid density at the interface, where the two fluids are equally mixed by volume (such that the mole fractions are equal). For certain classes of initial conditions, such as thermal equilibrium, M also determines the vertical variations of the equilibrium density and pressure profiles [10, 14]. In these cases, it can be regarded, in addition, as a stratification parameter [11].

2.2 Initial Conditions

The system is initialized with a hydrostatic background state, to which linear perturbation fields for density and pressure are added due to the interface perturbation. Alternatively, the modes can also be superimposed such that no perturbation is required for the interface, density, or pressure, but a linear perturbation field for velocity must be added.

The initial velocity field is zero, representing a system at rest. Plugging $u_i = 0$ into (2), the hydrostatic background state requires:

$$\frac{\partial p^H}{\partial x_1} = -\rho^H g. \tag{7}$$

Assuming a background state in thermal equilibrium, $T = T_0 = T_I$, the solution for each fluid is

$$\begin{aligned} p_m^H &= P_I \exp\left(-\frac{g x_1}{R_m T_0}\right), & (8)\\ \rho_m^H &= \frac{P_I}{R_m T_0} \exp\left(-\frac{g x_1}{R_m T_0}\right), & (9) \end{aligned}$$

where the subscript $m = \overline{1,2}$ describes the fluid species.

The nondimensional version of the background equilibrium state is

$$\begin{aligned} p_{1,2}^{H*} &= \exp\left[-M^2(1 \pm A)x_1\right], & (10)\\ \rho_{1,2}^{H*} &= (1 \pm A)\exp\left[-M^2(1 \pm A)x_1\right]. & (11) \end{aligned}$$

Figure 1 shows the background density profiles for various M and A. It is easily observed from the profiles and the analytical solution for the background density that M is a measure of stratification for this case. Additionally, the stratification is also strongly affected by A. At high values of A, the density profiles for the bottom fluid are largely unaffected by M, while the stratification in the top fluid is drastically affected by M.

A single-mode perturbation is added to the hydrostatic background state consistent with linear stability theory [10]. The perturbation fields for the two-dimensional system are of the form:

$$\begin{aligned} p'_m &= F_m(x_1)\exp(ikx_2 + nt), & (12)\\ \rho'_m &= G_m(x_1)\exp(ikx_2 + nt). & (13) \end{aligned}$$

The x_1-dependent functions are solved from the governing equations (1)-(3) with the imposed solution from (12) and (13) [10]. The initial fields for pressure and density for each fluid are then:

$$\begin{aligned} p_m &= p_m^H + p'_m, & (14)\\ \rho_m &= \rho_m^H + \rho'_m. & (15) \end{aligned}$$

The growth rate for the incompressible case is widely used and has the simple form

$$n = \sqrt{Agk}, \tag{16}$$

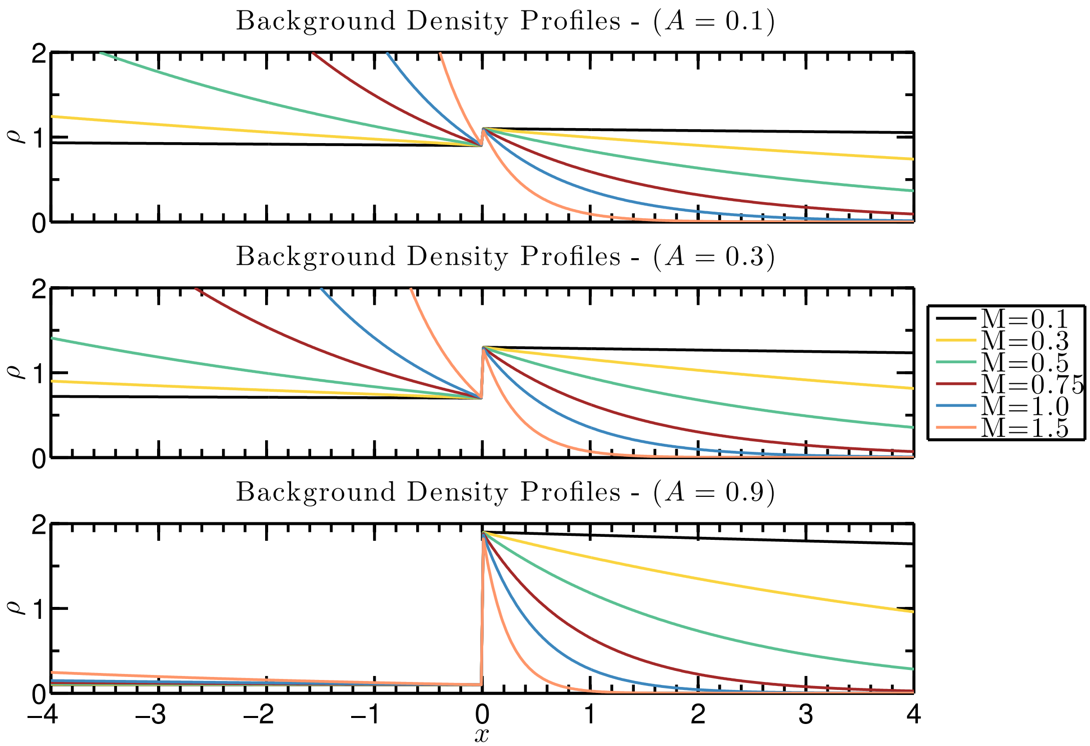

Figure 1: Background density profiles at various M and A for the thermal equilibrium case.

where k is the perturbation wavenumber. The linear stability analysis has been extended to find an upper bound for the growth rate taking into account the effects of viscosity and diffusivity for the incompressible case. The growth rate for the incompressible case with viscous and diffusive effects has the form

$$n = \left(\frac{Agk}{\psi} + \nu^2 k^4 \right)^{1/2} - (\nu + D)k^2, \tag{17}$$

where ν is the kinematic viscosity, ψ is an empirical function of A, k, and the initial diffusion thickness of the interface δ [15]. Viscosity and diffusivity inhibit growth for high wavenumbers. Thus, a most unstable wavenumber, k_u, corresponding to a most unstable wavelength λ_u, grows faster than all other wavenumbers. Also, diffusion effects prevent instability growth above a critical wavenumber, k_c, with associated wavelength λ_c. Since most theoretical and computational work on RTI focuses on the incompressible case, these are commonly used relationships for the linear growth. The extension of linear stability analysis to the compressible case has shown that the effects of compressibility on the early time growth rate cannot be represented by a single parameter [10]. The added complexity due to the effects of compressibility is expected to increase as the late time growth of RTI is investigated.

To ensure the initialization is well resolved, the interface is smoothed by setting the molar mass fraction to $X_1 = [1 \pm \mathrm{erf}((x_1 - \eta(x_2))/\delta)]/2$, where $\eta(x_2)$ represents the location of the perturbed interface. The initial fields are smoothed at the interface using the contribution of the pure fluid solution to the smoothed hydrostatic background state. That is,

$$p = p_1 \frac{p^H}{p_1^H} \quad \text{and} \quad \rho = \rho_1 \frac{\rho^H}{\rho_1^H} \quad \text{for} \quad x_1 - \eta(x_2) \geq 0, \tag{18}$$

$$p = p_2 \frac{p^H}{p_2^H} \quad \text{and} \quad \rho = \rho_2 \frac{\rho^H}{\rho_2^H} \quad \text{for} \quad x_1 - \eta(x_2) \leq 0, \tag{19}$$

where the smoothed equilibrium fields are given by

$$p^H = P_I \exp\left[\frac{-g}{RT_0}\left(x_1 - \eta(x_2) - \frac{\delta^2}{2}\frac{\partial \ln R}{\partial x_1}\right)\right], \tag{20}$$

$$\rho^H = \frac{p^H}{RT_0}. \tag{21}$$

The perturbed initial temperature is then derived from the equation of state.

For variable density flows in the limit of incompressible pure fluids, mixing by species diffusion leads to non-zero divergence of velocity [16], which is equivalent to

$$u_i = D\frac{\partial \ln R}{\partial x_i} \tag{22}$$

for the compressible case. When accounting for the initial diffusive mixing in the compressible case, there is no way to obtain a fully consistent initialization that accounts for both the species and enthalpy diffusion in the energy equation. Therefore, acoustic waves are necessarily generated from the initial conditions, whose magnitudes are dependent upon M, A, D, and the initial diffusive layer thickness, δ. The acoustic waves are greatly reduced by setting the initial velocity field to the diffusive mixing velocity given in equation (22). The initialization represents a slightly diffused interface before the perturbation is applied.

3 Numerical Implementation

The use of a wavelet-based adaptive method for the simulation of complex fluid systems permits efficient use of computational resources, since high resolution simulations are performed only where small structures are present in the flow. Representation of the flow using wavelets allows the grid to dynamically adapt to the structures in the flow as they evolve in time while maintaining a direct control of the error [17]. The Adaptive Wavelet Collocation Method is used in conjunction with non-reflecting boundary conditions developed for highly stratified systems. This combination allows for extremely long domains for isolating the growth of RTI with highly compressible, and thus stratified, fluids.

3.1 Adaptive Wavelet Collocation Method

The Adaptive Wavelet Collocation Method (AWCM) utilizes wavelets to locally adapt the numerical resolution during the evolution of complex flows [18, 19, 20]. Thus, localized structures are well-resolved while optimizing computational resources. In order to simplify the computation of nonlinear terms, a wavelet collocation method is used, which ensures a one-to-one correspondence between grid points and wavelets. Wavelets are functions that are localized in both wavenumber and physical space, which are used as a set of basis functions to represent the flow in terms of wavelet coefficients. In this sense, wavelets provide both frequency and position information about the flow. AWCM uses wavelet decomposition to determine those wavelets that are insignificant for representing the solution while maintaining a direct error control. Once scaling functions, $\phi^j_{\mathbf{k}}(\mathbf{x})$, and wavelet interpolating functions, $\psi^{\mu,j}_{\mathbf{l}}(\mathbf{x})$, are constructed [20], a function $f(\mathbf{x})$ can be decomposed as

$$f(\mathbf{x}) = \sum_{\mathbf{k}} c^0_{\mathbf{k}}\phi^0_{\mathbf{k}}(\mathbf{x}) + \sum_{j=0}^{\infty}\sum_{\mu=1}^{2^n-1}\sum_{\mathbf{l}} d^{\mu,j}_{\mathbf{l}}\psi^{\mu,j}_{\mathbf{l}}(\mathbf{x}). \tag{23}$$

A wavelet coefficient, $d^{\mu,j}_{\mathbf{l}}$, will have a small value unless the function varies on the scale j in the immediate vicinity of the wavelet $\psi^{\mu,j}_{\mathbf{l}}(\mathbf{x})$. For functions where isolated small structures exist on a large-scale background, most of the wavelet coefficients are small. The wavelets associated with coefficients less than a prescribed threshold parameter, ϵ, can be discarded in representing the solution, while retaining an approximation with an error that is $O(\epsilon)$. Derivatives are calculated at the corresponding local resolution using finite differences. Second-generation wavelets are used, which allow the order of the wavelets, and, thus, the order of the finite differences, to be easily varied.

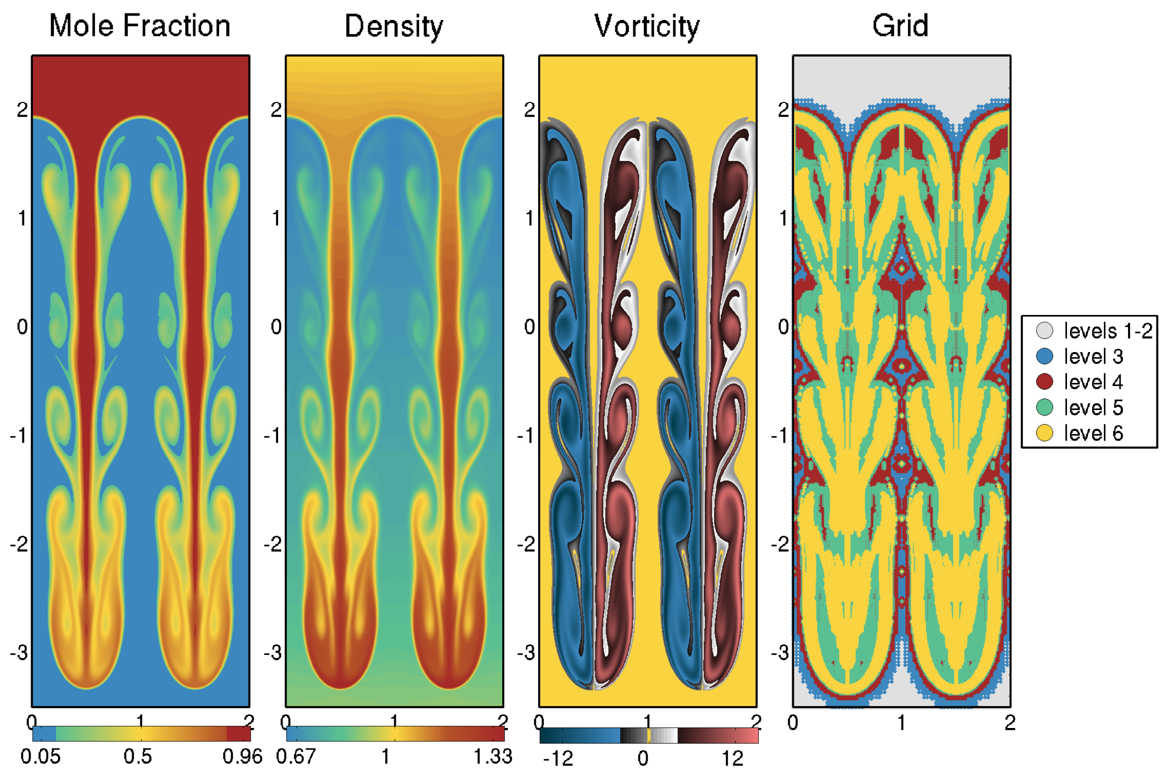

Figure 2: Mole fraction, density, vorticity, and the associated adaptive grid for the late-time instability growth with $M = 0.3$ and $A = 0.3$.

When solving evolution problems, such as the growth of Rayleigh-Taylor instability, an adjacent zone is added to the points associated with wavelets, whose coefficients are significant. By adding the nearest neighbors of the significant wavelet coefficients in both position and scale, the computational grid contains points that could become significant during a time step. The dynamic grid adaptation allows the efficient use of computational resources to resolve a wide range of scale structures as they evolve. A typical dynamically adapted grid is shown in Figure 2 for a late-time RTI simulation. The effective global resolution is 8193×512, yet only 16.5% of the points are used (690,318 points, 83.5% compression). Figure 3 shows the grid for highly stratified RTI. In this case, relatively strong acoustic waves are generated at the interface due to minimal, but unavoidable, inconsistencies in the initialization. The waves are clearly seen in the temperature field shown in the figure. AWCM dynamically adapts the computational mesh and resolves the acoustic waves as they travel outward from the initial interface. For this case, the effective global resolution is 8193×512, yet only 9% of the points are used (375,634 points, 91% compression).

Grid adaptation can be done in different ways. One way is simply to adapt on each integrated variable. Another method, used in this work, involves adaptation on additional dynamically important physical quantities, such as vorticity or strain rate, which ensures adequate resolution of the flow structures that control the dynamics of the flow evolution. Traditionally, the resolution studies for AWCM are performed by increasing and decreasing the threshold parameter, ϵ, while adjusting the maximum level of resolution and the number of wavelets used to represent the solution. In this study the convergence studies are performed by increasing and decreasing the effective resolution, while keeping ϵ constant. When, the maximum level, J, is increased by one, the effective resolution increases by a factor of two in each dimension. The results of the resolution study for the $A = 0.7$ case are presented in Figure 4. The solution is clearly converged as the effective resolution increases.

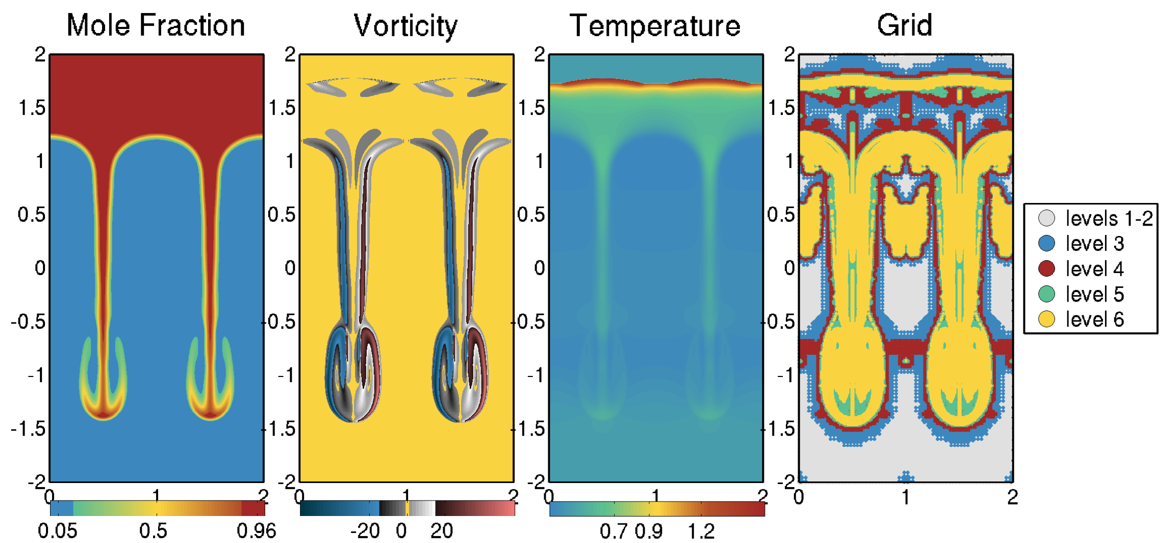

Figure 3: Mole fraction, vorticity, temperature, and the associated adaptive grid for RTI with a highly stratified background state ($M = 1.5$ and $A = 0.9$).

3.2 Non-Reflecting Boundary Conditions for Stratified Flow

The domain is periodic in the horizontal (x_2) direction. The boundary conditions in the vertical (x_1) direction are designed to simulate an infinite domain such that any pressure wave approaching the numerical boundaries is not reflected and, thus, does not interact with and disturb the growth of the instability. Acoustic waves are created at the interface at the initial time and travel in the vertical direction. The instability is isolated by applying non-reflecting characteristics-based boundary conditions at the top and bottom of the domain.

The non-reflecting characteristics-based boundary conditions are similar to the LODI conditions introduced by Poinsot and Lele [21]. However, a modification is required to account for the stratified background state. The analysis is performed on the one-dimensional Euler equations,

$$\frac{\partial \rho}{\partial t} + \rho \frac{\partial u}{\partial x} + u \frac{\partial \rho}{\partial x} = 0, \tag{24}$$

$$\frac{\partial u}{\partial t} + u \frac{\partial u}{\partial x} + \frac{1}{\rho} \frac{\partial p}{\partial x} = 0, \tag{25}$$

$$\frac{\partial p}{\partial t} + \rho c^2 \frac{\partial u}{\partial x} + u \frac{\partial p}{\partial x} = 0, \tag{26}$$

where c is the speed of sound. The waves are approximately planar and viscous effects are not considered. Pressure and density can be decomposed into the steady hydrostatic background state and the unsteady fields as follows:

$$p = p^H + \tilde{p}, \tag{27}$$

$$\rho = \rho^H + \tilde{\rho}. \tag{28}$$

The hydrostatic quantities have the relationship given in (7) and are assumed constant with time, but vary with x_1. Therefore, the hydrostatic background state is removed from the pressure and density evolution

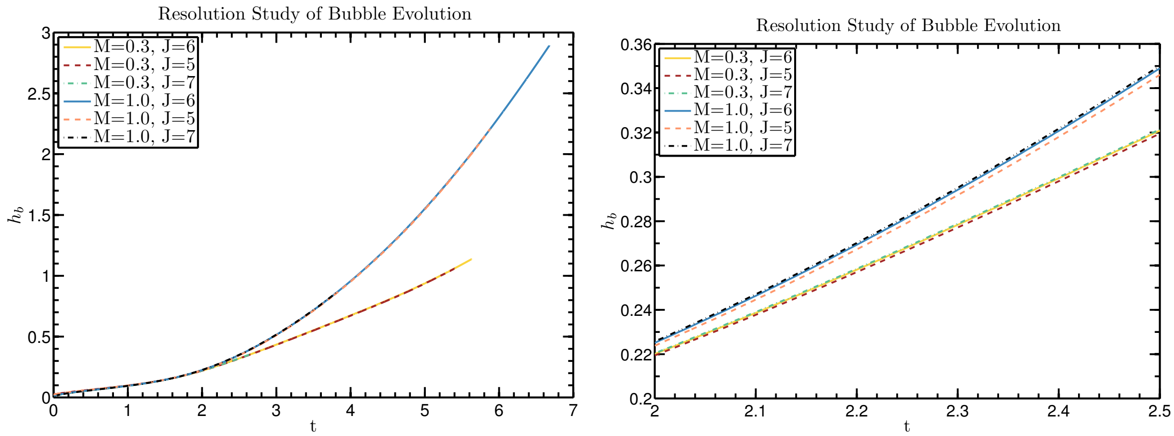

(a) Full evolution

(b) Zoomed in for observation

Figure 4: The results of the resolution study are shown for the entire bubble height evolution, as well as for a small window near the separation of the two bubble height line plots. J is the maximum number of resolution levels.

terms before the characteristic equations are derived. The modified Euler equations are:

$$\frac{\partial \tilde{\rho}}{\partial t} + \rho \frac{\partial u}{\partial x} + u \frac{\partial \tilde{\rho}}{\partial x} = -u \frac{\partial \rho^H}{\partial x}, \tag{29}$$

$$\frac{\partial u}{\partial t} + u \frac{\partial u}{\partial x} + \frac{1}{\rho} \frac{\partial \tilde{p}}{\partial x} = \frac{\rho^H g}{\rho}, \tag{30}$$

$$\frac{\partial \tilde{p}}{\partial t} + \rho c^2 \frac{\partial u}{\partial x} + u \frac{\partial \tilde{p}}{\partial x} = \rho^H g u. \tag{31}$$

The differential characteristic variables for this system are:

$$dv_1 = \rho c \, du - d\tilde{p}, \tag{32}$$

$$dv_2 = c^2 \, d\tilde{\rho} - d\tilde{p}, \tag{33}$$

$$dv_3 = \rho c \, du + d\tilde{p}, \tag{34}$$

which results with the following characteristic equations:

$$\frac{\partial v_1}{\partial t} + (u - c) \frac{\partial v_1}{\partial x} = -(u - c) \rho^H g, \tag{35}$$

$$\frac{\partial v_2}{\partial t} + u \frac{\partial v_2}{\partial x} = u(\gamma - 1) \rho^H g, \tag{36}$$

$$\frac{\partial v_3}{\partial t} + (u + c) \frac{\partial v_3}{\partial x} = (u + c) \rho^H g. \tag{37}$$

Therefore, the LODI conditions are applied only to the unsteady fields, and the hydrostatic background state affects the system through appropriate source terms in the characteristic equations. The incoming characteristics are set to zero for non-reflecting boundary conditions. In order to ensure a well-posed system consistent with the LODI conditions while considering a viscous flow, the x_1 spatial derivatives of the tangential stresses, normal heat flux, and normal species flux are set to zero at the boundaries.

4 Results

A previous study of the incompressible case has shown that AWCM successfully captures the linear regime, bubble and spike formations, and late-time flow characteristics for the single-mode perturbation case [22].

An extension of that study is presented here, where the compressibility effects on the single-mode RTI are investigated across a wide span of interfacial density ratios. For all cases, the viscosity is set based on the perturbation Reynolds number, $Re_p = 1500$, where

$$Re_p = \sqrt{\frac{Ag\lambda^3}{(1+A)\nu^2}}. \tag{38}$$

A summary of results is given in Figure 5, where bubble height, spike height, bubble velocity, and spike velocity are shown for various M values for each A under investigation. Most of the cases show an early diffusive region, followed by a linear growth phase. In the early nonlinear stages, the vorticity is still small and the instability can be described using potential flow theory and a simple buoyancy-drag model [23, 24]. In the asymptotic limit of this model, where the buoyancy and drag effects are balanced, a constant bubble and spike velocity can be calculated as

$$V_{b/s} = \left[\frac{2A}{(1 \pm A)}\frac{g\lambda}{C_d}\right]^{1/2}, \tag{39}$$

where the drag coefficient is determined from the bubble terminal velocity relationships for the $A = 1$ limit, which gives $C_{d_{2D}} = 6\pi$ and $C_{d_{3D}} = 2\pi$. Until recently, this was called the terminal or asymptotic velocity, since it was believed to describe the late time behavior of single-mode RTI. However, as vorticity is generated by the Kelvin-Helmholtz instability on the sides of the bubbles and spikes, such a description becomes inadequate. Indeed, the late time growth varies considerably from the potential flow description, which is obvious from the cases considered here. The behavior of the higher-M cases depends on the Atwood number. At low-A ($A = 0.1$), increasing the compressibility (going to higher M) results in a drastic decrease in the overall growth on both the bubble and spike sides of the interface. For the moderate $A = 0.3$ case, the trend observed in the $A = 0.1$ case begins to diminish, since all but the highest M case converge until the well into the reacceleration phase. During the reacceleration phase, the higher M cases do become suppressed. As the Atwood number is increased even further, the behavior of the bubble at high-M reverses. That is, at high-A, increasing the compressibility effects enhances the growth rate. It must be noted that the enhancement only occurs on the bubble side, since the spike velocities converge at high A. Also, the increased growth at high-A and high-M only occurs when the lower compressibility cases enter the deceleration stage.

In order to observe the stratification effects on the growth of the instability as M is varied, Figure 7 compares the $M = 0.3$ and $M = 1.0$ cases for $A = 0.1$. At low A, the stratification is about the same on both sides of the interface, since there is very little density difference. For low-M and low-A, the heavy fluid is compressed as it falls, while the density in the light fluid decreases as it rises. This maintains an unstable situation as the instability grows. For high-M and low-A, the initial density difference at the interface is small when compared to the background stratification. The spike only falls a short distance before global stability is achieved.

Figure 7 shows results for the moderate $A = 0.3$ case. Once again, the background stratification is vastly different between the $M = 0.3$ and $M = 1.0$ cases. Also, the shapes of the bubbles and spikes are considerably unique. Despite these differences, the growth of the instability is largely the same for both the bubbles and the spikes until a relatively late time, when spike height reaches 2.5λ. At that point, the high-M cases is once again suppressed. The behavior at $A = 0.3$ is similar to, but delayed with respect to, the $A = 0.1$ case.

The large density difference case is presented in Figure 8, where $A = 0.7$. There are differences in the background stratification, but most of the variance occurs in the top fluid. Since, the lower fluid's molar mass is much smaller than that of the top fluid, the densities are much smaller, which leads to relatively low stratification. Thus, the lower fluid is largely unaffected by the compressibility effects, which explains the moderate convergence of spike velocities in the high-A regime. Although the spike velocities for all M approach the $M = 0.1$ curve, the incompressible case remains the upper bound for the growth of the spike. Conversely, the growth of the bubble increases with M, as observed in Figure 8.

5 Conclusion and Future Work

The use of AWCM for direct numerical simulations of Rayleigh-Taylor systems is ideal, since the spatial localization of the mixing layer leads to significant compression in the number of points necessary, while maintaining a high effective resolution and an explicit error control. The combination of AWCM with non-reflecting boundary conditions suited for stratified systems ensures the optimal use of computational resources while isolating the growth of highly compressible RTI. Compressibility affects RTI in many distinct ways. Acoustic waves are generated from the interface at early times and throughout the growth of the instability. Minimizing their impact on the uninhibited development of the Rayleigh-Taylor mixing layer is the goal here. However, RTI interaction with acoustic waves may have noticeable effects in many real systems. The stratification within a Rayleigh-Taylor system is interrelated with the acoustic and material properties of the fluids. Stratification effects can either suppress or enhance the growth of RTI, depending upon the molar mass ratio of the pure fluids. Furthermore, the suppression or enhancement may be different on the two sides of the interface. For the thermal equilibrium case presented here, the background stratification acts to suppress the instability growth when the molar masses are similar. In order to make inertial confinement fusion a viable energy resource, various methods of suppressing RTI must be explored. For cases with large molar mass differences, the stratification is found to enhance the growth of the bubble, while the growth of the spike converges to the incompressible case. Compressibility likely plays a large role in most systems that involve RTI in nature, such as supernovae explosions and atmospheric flows. In order to continue this investigation into an area of such pressing needs, the vortex dynamics must be explored to obtain a full understanding of the compressibility effects at late times.

This work was made possible by funding from the LDRD program at Los Alamos National Laboratory through project numbers 20070195ER and 20090058DR.

References

[1] S Chandrasekhar. *Hydrodynamic and Hydromagnetic Stability.* (New York: Dover), 1981.

[2] L Rayleigh. Investigation of the character of the equilibrium of an incompressible heavy fluid of variable density. *Proc. R. Math. Soc.*, **14**:170–7, 1883.

[3] G Taylor. The instability of liquid surfaces when accelerated in a direction perpendicular to their planes .1. *Proc. R. Soc. London, Ser. A*, **201**:192–6, 1950.

[4] D L Youngs. Numerical-simulation of turbulent mixing by Rayleigh-Taylor instability. *Physica D*, **12**:32–44, 1984.

[5] B A Remington, S V Weber, M M Marinak, S W Haan, J D Kilkenny, R J Wallace, and G Dimonte. Single-mode and multi-mode Rayleigh-Taylor experiments on NOVA. *Phys. Plasmas*, **2**:241–55, 1995.

[6] D R Farley and L M Logory. Single-mode, nonlinear mix experiments at high Mach number using Nova. *Astrophys. J. Suppl. Ser.*, **127**:311–6, 2000.

[7] J D Kilkenny, S G Glendinning, S W Haan, B A Hammel, J D Lindl, D Munro, B A Remington, S V Weber, J P Knauer, and C P Verdon. A review of the ablative stabilization of the Rayleigh-Taylor instability in regimes relevant to inertial confinement fusion. *Phys. Plasmas*, **1**:1379–89, 1994.

[8] J P Knauer, R Betti, D K Bradley, T R Boehly, T J B Collins, V N Goncharov, P W McKenty, D D Meyerhofer, V A Smalyuk, C P Verdon, S G Glendinning, D H Kalantar, and R G Watt. Single-mode, Rayleigh-Taylor growth-rate measurements on the OMEGA laser system. *Phys. Plasmas*, **7**:338–45, 2000.

[9] W H Cabot and A W Cook. Reynolds number effects on Rayleigh-Taylor instability with possible implications for type-Ia supernovae. *Nat. Phys.*, **2**:562–8, 2006.

[10] D. Livescu. Compressibility effects on the Rayleigh-Taylor instability growth between immiscible fluids. *Phys. Fluids*, **16**:118–27, 2004.

[11] S. Gauthier and B. Le Creurer. Compressibility effects in Rayleigh-Taylor instability-induced flows. *Philos. Trans. R. Soc. London, Ser. A*, **368**:1681–704, 2010.

[12] D. Livescu, J. R. Ristorcelli, R. A. Gore, S. H. Dean, W. H. Cabot, and A. W. Cook. High-Reynolds number Rayleigh-Taylor turbulence. *J. Turbul.*, **10**:1–32, 2009.

[13] F A Williams. *Combustion Theory.* (Menlo Park: Benjamin/Cummings), 1985.

[14] H Yu and D Livescu. Rayleigh-Taylor instability in cylindrical geometry with compressible fluids. *Phys. Fluids*, **20**, 2008.

[15] R E Duff, F H Harlow, and C W Hirt. Effects of diffusion on interface instability between gases. *Phys. Fluids*, **5**:417–25, 1962.

[16] D Livescu and J R Ristorcelli. Buoyancy-driven variable-density turbulence. *J. Fluid Mech.*, **591**:43–71, 2007.

[17] K. Schneider and O. V. Vasilyev. Wavelet methods in computational fluid dynamics. *Annu. Rev. Fluid Mech.*, **54**:473–503, 2010.

[18] O V Vasilyev and S Paolucci. A fast adaptive wavelet collocation algorithm for multidimensional PDEs. *J. Comput. Phys.*, **138**:16–56, 1997.

[19] O V Vasilyev and C Bowman. Second-generation wavelet collocation method for the solution of partial differential equations. *J. of Comput. Phys.*, **165**:660–93, 2000.

[20] O V Vasilyev. Solving multi-dimensional evolution problems with localized structures using second generation wavelets. *Int. J. of Comput. Fluid Dyn.*, **17**:151–68, 2003.

[21] T J Poinsot and S K Lele. Boundary-conditions for direct simulations of compressible viscous flows. *J. Comput. Phys.*, **101**:104–29, 1992.

[22] S J Reckinger, D Livescu, and O V Vasilyev. Adaptive wavelet-collocation method simulations of Rayleigh-Taylor instability. *Phys. Scr.*, **T142**, 2010.

[23] V N Goncharov. Analytical model of nonlinear, single-mode, classical Rayleigh-Taylor instability at arbitrary Atwood numbers. *Phys. Rev. Lett.*, **88**, 2002.

[24] D Oron, L Arazi, D Kartoon, A Rikanati, U Alon, and D Shvarts. Dimensionality dependence of the Rayleigh-Taylor and Richtmyer-Meshkov instability late-time scaling laws. *Phys. Plasmas*, **8**:2883–9, 2001.

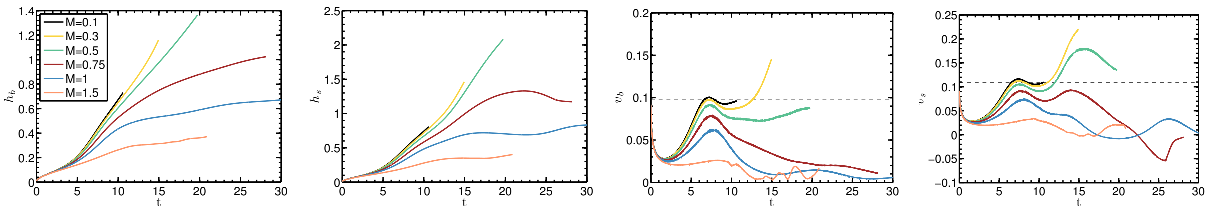

(a) h_b evolution, $A = 0.1$ (b) h_s evolution, $A = 0.1$ (c) v_b evolution, $A = 0.1$ (d) v_s evolution, $A = 0.1$

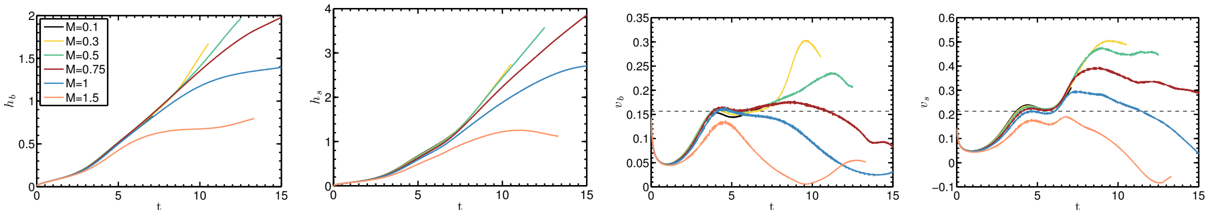

(e) h_b evolution, $A = 0.3$ (f) h_s evolution, $A = 0.3$ (g) v_b evolution, $A = 0.3$ (h) v_s evolution, $A = 0.3$

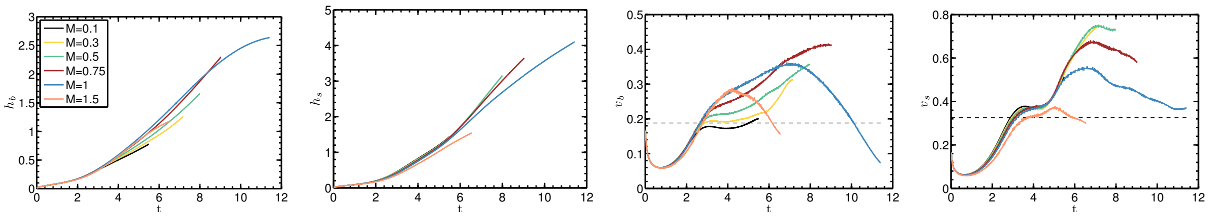

(i) h_b evolution, $A = 0.5$ (j) h_s evolution, $A = 0.5$ (k) v_b evolution, $A = 0.5$ (l) v_s evolution, $A = 0.5$

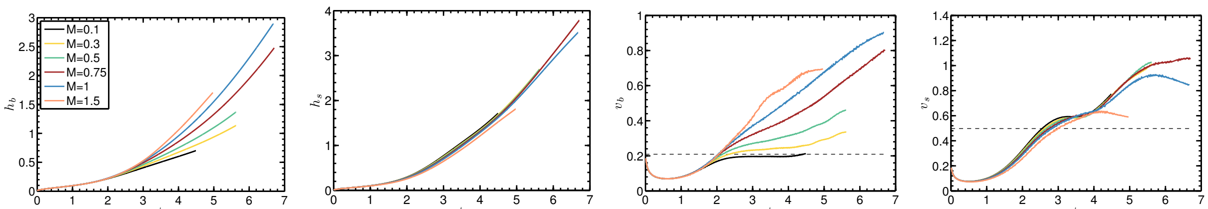

(m) h_b evolution, $A = 0.7$ (n) h_s evolution, $A = 0.7$ (o) v_b evolution, $A = 0.7$ (p) v_s evolution, $A = 0.7$

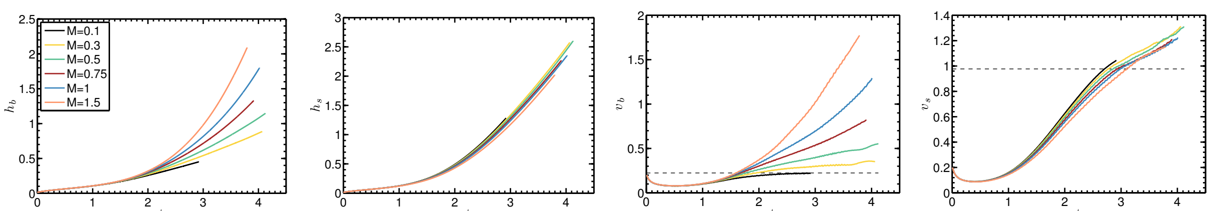

(q) h_b evolution, $A = 0.9$ (r) h_s evolution, $A = 0.9$ (s) v_b evolution, $A = 0.9$ (t) v_s evolution, $A = 0.9$

Figure 5: The M-dependence of the evolutions of bubble height, h_b (far left column), spike height, h_s (second column), bubble velocity, v_b (third column), and spike velocity, v_s (far right column) are shown for various A (rows). The dotted line represents the asymptotic velocity values from potential flow theory.

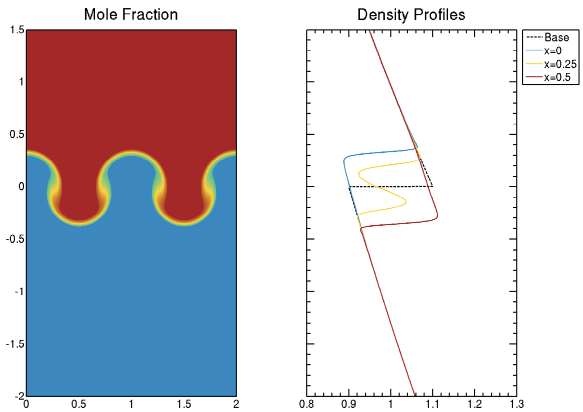

(a) $h_s = 0.4$ for $M = 0.3$

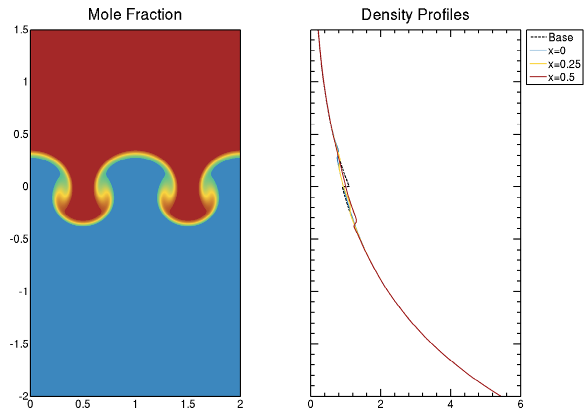

(b) $h_s = 0.4$ for $M = 1.0$

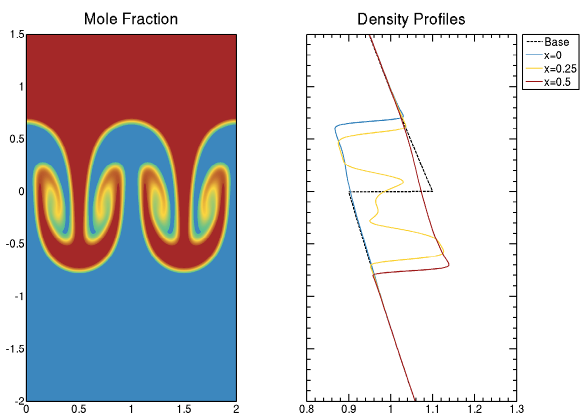

(c) $h_s = 0.8$ for $M = 0.3$

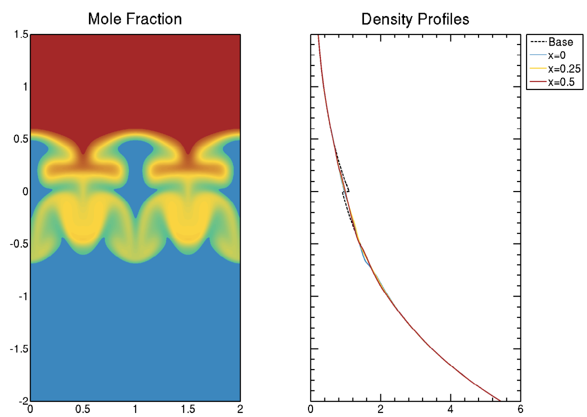

(d) $h_s = 0.8$ for $M = 1.0$

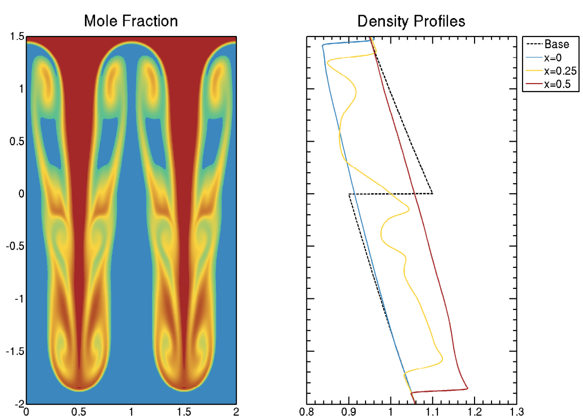

(e) Late-time for $M = 0.3$

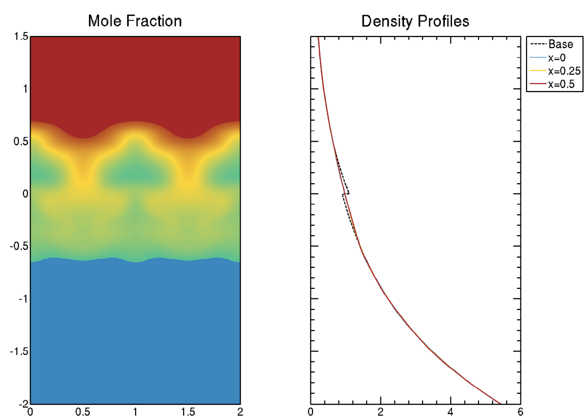

(f) Late-time for $M = 1.0$

Figure 6: Mole fraction and density profiles for $A = 0.1$, at $M = 0.3$ (low compressibility) and $M = 1.0$ (high compressibility) for comparison.

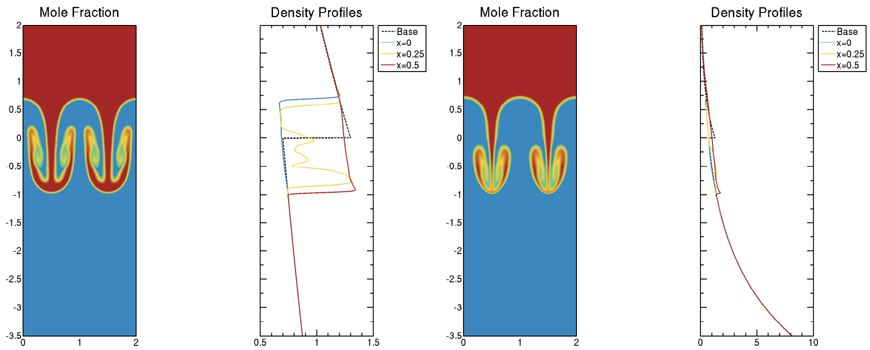

(a) $h_s = 1.0$ for $M = 0.3$ (b) $h_s = 1.0$ for $M = 1.0$

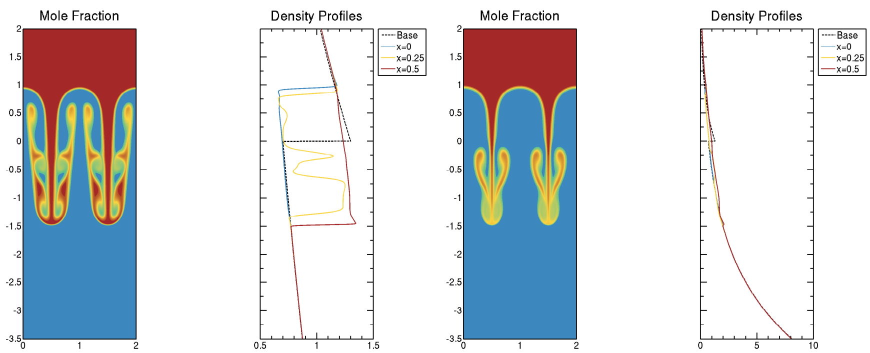

(c) $h_s = 1.5$ for $M = 0.3$ (d) $h_s = 1.5$ for $M = 1.0$

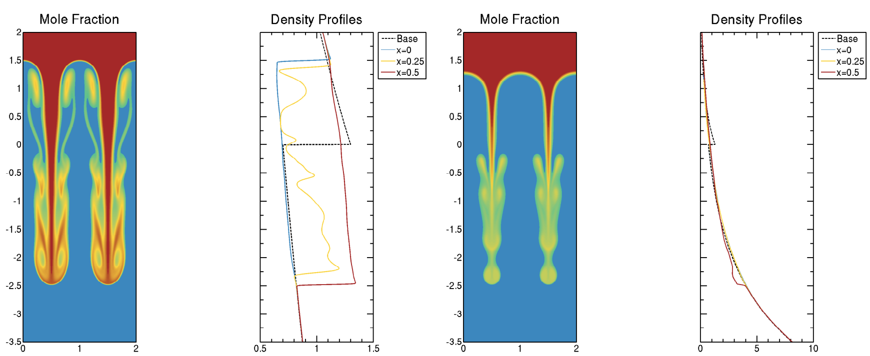

(e) $h_s = 2.5$ for $M = 0.3$ (f) $h_s = 2.5$ for $M = 1.0$

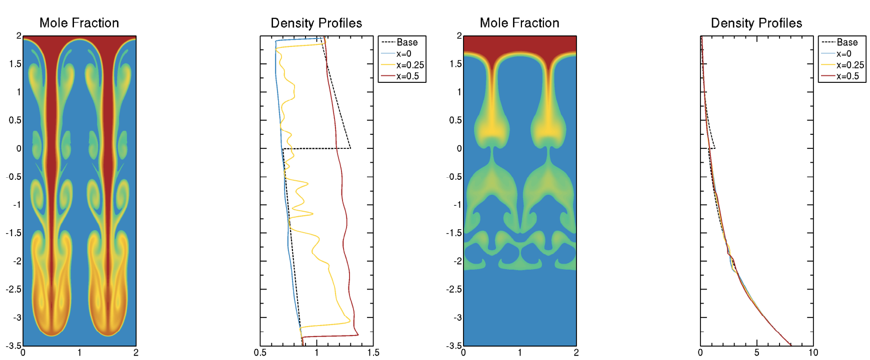

(g) Late-time for $M = 0.3$ (h) Late-time for $M = 1.0$

Figure 7: Mole fraction and density profiles for $A = 0.3$, at $M = 0.3$ (low compressibility) and $M = 1.0$ (high compressibility) for comparison.

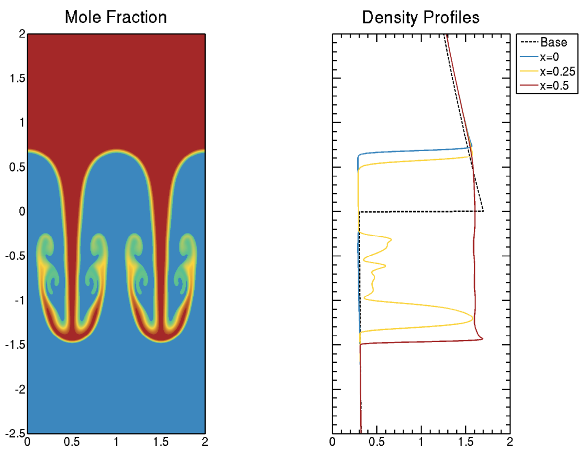

(a) $h_s = 1.5$ for $M = 0.3$

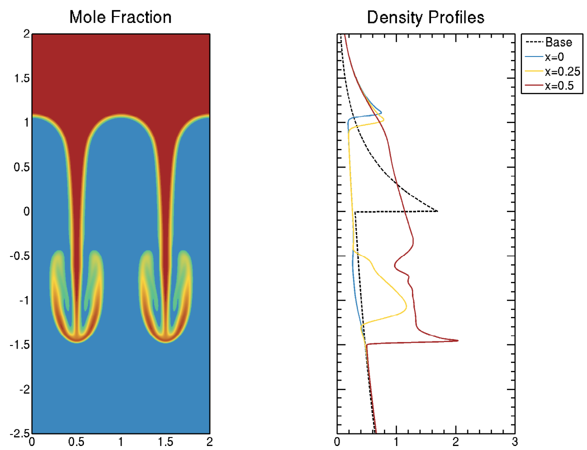

(b) $h_s = 1.5$ for $M = 1.0$

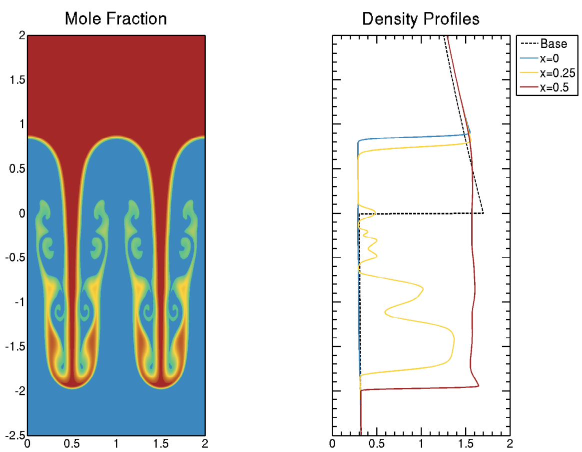

(c) $h_s = 2.0$ for $M = 0.3$

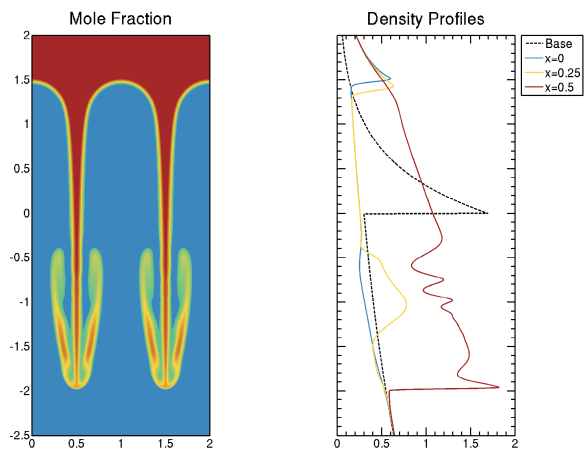

(d) $h_s = 2.0$ for $M = 1.0$

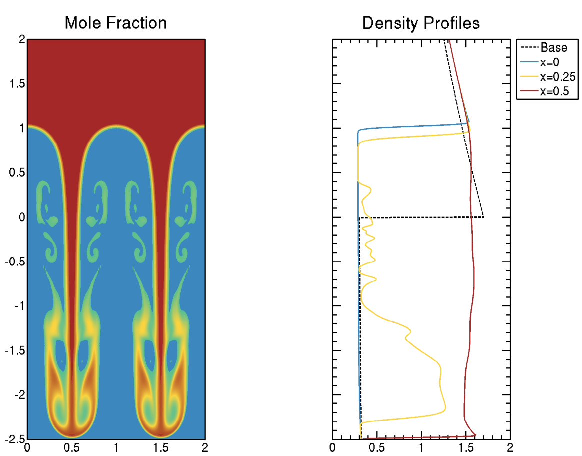

(e) $h_s = 2.5$ for $M = 0.3$

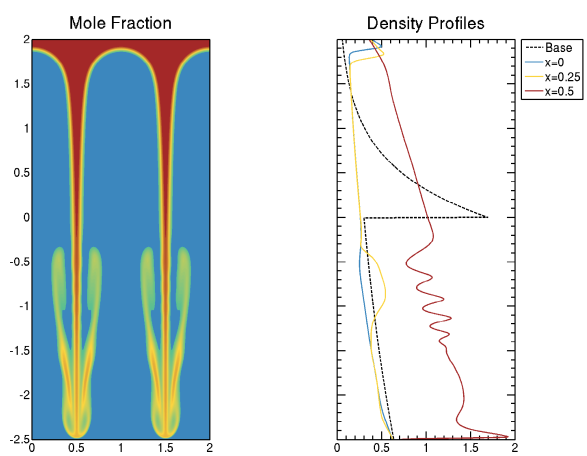

(f) $h_s = 2.5$ for $M = 1.0$

Figure 8: Mole fraction and density profiles for $A = 0.7$, at $M = 0.3$ (low compressibility) and $M = 1.0$ (high compressibility) for comparison.